

Two-Axis MOEMS Sun Sensor for Pico Satellites

Jan H. Hales and Martin Pedersen
Mikroelektronik Centret (MIC)
Technical University of Denmark (DTU)
Advisor – Process Specialist M.Sc. René Fléron

Abstract

A MOEMS sun sensor has been designed for DTUsat – a Danish student CubeSat project at the Technical University of Denmark. On the magnetotorquer controlled DTUsat sun sensors are needed along with a magnetometer to obtain unambiguous attitude determination for the ACDS and the payloads – an electrodynamic tether and a camera. Due to requirements such as low mass, high accuracy, and high FOV a solution different from the currently available is needed. By utilising resources from space and micro processing related fields a SOI based two-axis linear slit sensor chip with $\pm 70^\circ$ FOV and a theoretical resolution of $\sim 0.07^\circ$ has been designed. The chip design enables elimination of various ambient factors such as e.g. temperature and cosine dependencies. This paper describes design, functionality, and process sequence of the device. A PCB with the chip and measuring electronics has been designed with a mass below 3g.

1 Introduction

Miniaturisation of mechanics and integration with electronics in MEMS¹ devices allows construction of low-power robust satellite systems that are much smaller than conventional systems. When a MEMS replace a conventional electro-mechanical system the mass is often reduced to 0.05-1%. Utilisation of MEMS in space applications is however still limited. MEMS is especially interesting for very small spacecrafts used as e.g. measuring probes ejected from larger spacecrafts.

For the DTUsat mission² small sub-systems are needed due to the desire of an advanced platform, relative heavy payloads, and the constraint that the satellite is a pico satellite. Because of this two MEMS devices are being developed for the mission. One is a MOEMS³ sun sensor, and the other is an electron emitter needed as part of the payload. This article describes the sun sensor, for which the design has been finished.

Before beginning the description of the sun sensor an overview is given of the DTUsat project. This includes the platform, payloads and the ACDS.

¹MEMS: Micro-Electro-Mechanical-System.

²<http://www.dtusat.dtu.dk/>

³MOEMS: Micro-Opto-Electro-Mechanical-System.

1.1 The DTUsat project

The DTUsat project is a pure student project at the Technical University of Denmark (DTU). The students define their own projects, and are involved in everything from funding to fabrication via design. The faculty staff is of course still attached as advisors, and they also bring their ideas, suggestions etc. to meetings in the system engineering committee – where students coordinate projects, define interfaces, keep track of budgets (financial, power, weight, size) etc. The goal of this management method is to implement education within more areas than the specific area of each student's project.

The DTUsat project was started in 2001 and currently ~ 40 DTU students, and a few from Copenhagen University, are involved. Launch for DTUsat is expected in early summer 2003 – expected altitude is 650km. Since DTUsat is a CubeSat it will of course fulfill the CubeSat requirements (e.g.: 10cm cube, 1kg). The specifications for DTUsat can be seen in table 1.

1.2 Payloads

DTUsat carries three payloads, namely an electrodynamic tether, a camera, and a radio test broadcaster. The radio test broadcaster sends out a sequence of messages that decreases in signal ampli-

Mechanical	Meets CubeSat spec.
On Board Computer	32bit RISC ATMEL CPU (operating at 15MHz) 16Mbit Flash 8Mbit RAM 128kbit PROM
Radio	9600bps, GMSK
Antenna	Omnidirectional Circular Polarisation (Turnstile)
Power	1-2W
Software	OS: Redhat eCos Module oriented software platform with internal communication via a packet router.

Table 1: Platform specification.

tude. This will help radio amateurs to test their equipment. In return for this service AMSAT⁴ provides the DTUosat team with a radio frequency.

The camera payload consists of a CCD camera, which will produce pictures of Denmark. The resolution of the camera will be 640×480 pixels, and it will produce pictures corresponding to $482\text{km} \times 336\text{km}$ of land in each photography – yielding 750m resolution. The system is designed to be capable of taking pictures at night. The camera payload requires attitude estimates from the ACDS, and a spin rate of $< 0.05 \frac{\text{rad}}{\text{s}}$ with respect to a fixed point on the surface of Earth.

The tether payload consists of a 700m long wire with a diameter of 0.2mm. Electrons will be emitted from the satellite and collected on the tether. This causes a current loop to be closed in the plasma, which will then expose DTUosat to a net force due to the interaction with the geomagnetic field. A 10km change of altitude within one year is the goal. However, the deployment of the tether is a difficult task, therefore several criteria of success have been made. The tether requires attitude estimates and:

- $\pm 10^\circ$ attitude pointing in the orbit plane before deployment.
- As low rotation as possible outside the orbit plane when the tether is ejected.
- Continues updates of centre of mass and moments of inertia by ACDS during deployment.
- Attitude change of $15^\circ - 30^\circ$ in the orbit plane is allowed during deployment.

⁴AMSAT: AMateur SATellite corporation.

- Damping or if possible active control of rotation about the tether axis when deployed.

1.3 The ACDS on DTUosat

Evaluation of different sensors and actuators with respect to the prior stated requirements and constraints of DTUosat have been made. The main points resulting from the analysis are depicted in table 2.

Sensor	Weight	1	2	3	4	5
Mass	2	-	++	0	-	0
Size	1	-	++	0	--	0
Power	2	-	++	+	-	-
Accuracy	1	-	+	++	++	--
Feasibility	3	0	+	++	--	++
Const. Risk	2	++	-	+	--	0
Op. Risk	3	--	+	++	-	++
De-tumbling	2	+	0	+	-	++
Add. Sensor	2	++	+	-	++	--
Result		-2	17	17	-15	8

Table 2: Trade off between different attitude sensors. Evaluated sensors: 1. Earth sensor, 2. Sun sensor, 3. Magnetometer, 4. GPS, and 5. Rate gyro.

The magnetometer and the sun sensor scores highest in the trade off table. Since none of them alone can be used to achieve unambiguous attitude determination they are both selected.

A four-axis magnetometer with a range of $60\mu\text{T}$ and an accuracy of $\pm 50\text{nT}$, corresponding to 0.16° , have been designed and constructed. The sensor has been exposed to 10krad and showed no defects or increase in supply current.

	Weight	1	2	3	4
Mass	2	++	+	0	-
Size	1	0	+	-	--
Power	2	++	+	+	-
Precision	2	0	0	+	++
Feasibility	3	0	++	+	--
Construction Risk	3	--	-	0	+
Operation Risk	3	++	+	0	-
Payload Compatibility	2	--	--	0	++
Sensor Compatibility	2	--	--	-	+
Result		0	3	4	-2

Table 3: Trade off between the different stabilisation and control types, where the different actuators are: 1. Pas. damped magnet, 2. Act. damped magnet, 3. Mag. torquers, and 4. Fly wheels.

Table 3 shows a similar evaluation carried out for relevant actuators. The trade off result is in favour of magnetotorquers. Magnetotorquers allow both simple two-axis and more advanced three-axis

control. The simple two-axis controller operates very similar to an active damped permanent magnet, but allows rotation of the permanent offset field to meet the tether requirements. The controller designed for DTUosat operates using this principle. Tumbling at the poles can also be avoided with magnetotorquers.

The design of the three-axis magnetotorquers has been carried out with respect to power, size and mass constrains. Resulting in a configuration with a total weight of 40g and capable of producing a torque of 0.6–1.5 μ Nm (depending on the magnitude of the geomagnetic field).

1.3.1 Control law

The control principle chosen is B-dot control, which is a suitable choice considering the sensors and actuators selected. In B-dot control the gradient of the measured magnetic field of the Earth is used as rate feedback to obtain a stabilised satellite, and an additional constant magnetic dipole moment is generated to align the satellite with the magnetic field – much like a permanent magnet.

The control torque for a magnetic controlled satellite can be expressed as:

$$\begin{aligned}
 \boldsymbol{\tau}_c &= \mathbf{m}_c \times \mathbf{B}^s \\
 &= k' \dot{\mathbf{B}}^s \times \mathbf{B}^s \\
 &= \frac{k}{|\mathbf{B}|^2} \dot{\mathbf{B}}^s \times \mathbf{B}^s \\
 &\approx \frac{k}{|\mathbf{B}|^2} (\boldsymbol{\omega} \times \mathbf{B}^s) \times \mathbf{B}^s \\
 &= -k \left(\mathbf{I}_{3 \times 3} - \frac{\mathbf{B}\mathbf{B}^T}{|\mathbf{B}|^2} \right) \boldsymbol{\omega} \quad (1)
 \end{aligned}$$

where index s denotes satellite coordinate frame. It can be seen from (1), that a satellite with e.g. the x -axis aligned with the magnetic field will not be able to counteract any angular velocity about this axis, as the resulting $\tau_{c,x} = 0$. Hence rotation about the axis of alignment cannot be damped by using magnetotorquers if perfect alignment is maintained.

In the long term this can result in a slow spin up of the satellite, when a constant magnetic dipole moment is utilised for alignment with the magnetic field. One solution to this spin up is finding a compromise between alignment and spin; a large constant dipole moment results in precise alignment but allows the satellite to spin, whereas a small constant dipole moment results in some misalignment which can be used for spin damping.

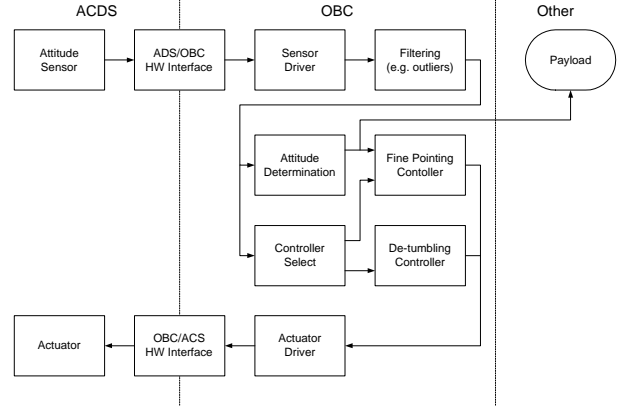


Figure 1: Block diagram of control system.

The control system can be split into a number of blocks as illustrated in figure 1.

The sensor outputs are transferred to the OBC⁵. Drivers handle updates of measurements and sensor schemes for making measurements. Output from the drivers will contain noise and outliers, so filtering is needed before the sensor output is used for control purposes and attitude determination. This is often implemented with a Kalman filter to make the controller robust to e.g. outliers.

Attitude information is required by the payloads and for fine pointing. This information is obtained by comparing sensor output with environment models for sun position and geomagnetic field.

Two attitude controllers can be used – a simple for de-tumbling, or a more complex for fine pointing. The fine pointing controller however has not yet been designed.

The required control torque expressed as a control signal is converted to a PWM⁶ signal by the actuator driver and the hardware interface.

Finally the PWM signal is used for driving the magnetotorquers generating the demanded magnetic dipole moment. The attitude determination and the actuator system designed are well within the requirements from the payloads and are designed to be versatile in order to support different payload platforms. This means that a change in payload mainly requires a change in the control algorithms. Rendering the determination system suitable for future DTUosat missions.

⁵OBC: On-Board Computer.

⁶PWM: Pulse Width Modulation.

2 Sensor Principle

Figure 2 shows the general design of the analog slit sun sensor that has been designed for DTUosat. The sensor is a composition of a Pyrex glass wafer on top of a SOI⁷ wafer. A SOI wafer is used since it enables electrical insulation by etching away the top mono-crystalline *Si*-layer, see figure 2 a).

The principle of the sensor is that sun rays enter the slit, which has width a , and generate a current in the three solar cell areas. The angle α_i of the incoming light can then be computed from the difference between the generated current in the two triangular cells. The rectangular cell is a reference used to eliminate e.g. ambient dependencies.

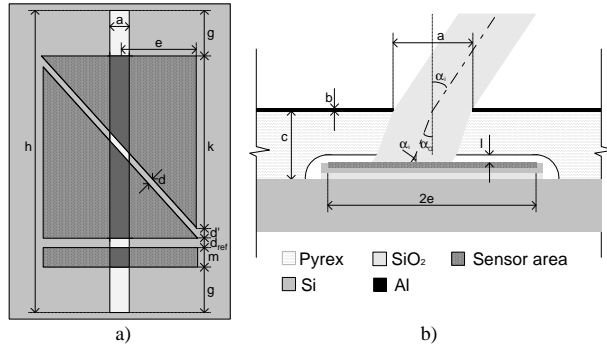


Figure 2: Sketch of the sun sensor. a) top view, b) cross sectional view.

Since DTUosat is cubic complete coverage can be obtained by designing for $\pm\text{FOV}^8 > \arctan(\sqrt{2a^2/a}) = 54.74^\circ \approx 55^\circ$ and placing one two-axis sensor on each of the satellite's sides. A two-axis sensor can be obtained by placing two of the sensors from figure 2 perpendicular to each other as seen in the chip layout in figure 10.

The solar cells will be implemented as pn junctions where photo currents can be generated. This happens when photons excite electrons into the valence band – creating electron-hole pairs. The electric field in the space charge region affects the electrons, and a reverse bias photo current I_{ph} is created. This current builds up a potential across the load, which will lower the E -field in the space charge region and cause a forward bias current I_f . Net generated current is then $I = I_{ph} - I_f$, where I_f is given by the ideal diode equation $I_f = I_s[\exp(\frac{eV}{kT}) - 1]$.

⁷SOI: Silicon On Insulator. It consists of *Si* – *SiO*₂ – Bulk-*Si* layers.

⁸FOV: Field Of View.

Where e is the electron charge, V forward voltage, k Boltzmann's constant, and T temperature.

Generated current in a triangular cell is given by:

$$I_t = \frac{\frac{P}{A} A_t(\alpha) \cos(\alpha_k) \cos(\alpha_e)}{V(T)} \eta \quad (2)$$

where $\frac{P}{A}$ is the sun power per square metre at the satellite, $A_t(\alpha)$ illuminated area of one triangle, $V(T)$ the diode forward voltage, and η the efficiency of the solar cell. The two α_x angles are the sun rays angles about the k and e axes.

The length of g is selected so that the illuminated area is independent of the α_e angle.

2.1 Unwanted Parameters

Several unwanted parameters can be cancelled out by dividing (2) with a reference signal obtained from the rectangular reference area – since this area has the same physical properties. The reference area has constant illuminated area $A_{ref} \approx am$. If the difference between the generated currents in the two triangular cells is used to find α then by division:

$$\begin{aligned} \frac{\Delta I}{I_{ref}} &= \frac{I_{t2} - I_{t1}}{I_{ref}} \\ &= \frac{\frac{P}{A} \cos(\alpha_a) \cos(\alpha_b) \eta (A_{t2}(\alpha) - A_{t1}(\alpha))}{\frac{P}{A} A_{ref} \cos(\alpha_a) \cos(\alpha_b) \eta} \\ &= \frac{A_{t2}(\alpha) - A_{t1}(\alpha)}{A_{ref}} \end{aligned} \quad (3)$$

This makes the sensor independent of the cosines and the temperature in $V(T)$ – cancelling of $V(T)$ also removes most dark current effects. Cancellation of η removes dependence of sensor degradation due to radiation. Elimination of $\frac{P}{A}$ cancels disturbances caused by sun power fluctuations, and albedo from the Earth⁹.

When (3) is used the output signal is only a function of the illuminated areas in the ideal case.

In excess of eliminating various ambient factors the reference area can also be used as a temperature sensor. An angle measurement allows calculation of the effect the sensor is exposed to since the sun power is relatively constant over time. Now it is possible to determine the temperature via the sensor's temperature dependence – this can be carried out analytically or from measured characteristics.

⁹Only the intensity contribution is eliminated.

2.2 A Digital Approach

A digital sun sensor, see figure 3, has also been included in the chip design. This sensor is made independent of albedo from the Earth and other dependencies by comparing currents from each bit with the ATA¹⁰ current. A bit is set if the generated current is the double of the ATA current since the ATA height is half the height of the bits. The sensor do however have the major drawback that its dimensions increases by $O(2^{n-1})$ with the desired bit resolution n .

The analog sensor is the sensor that will be used on DTUosat. Because of this the digital sensor will only be described briefly throughout this article.

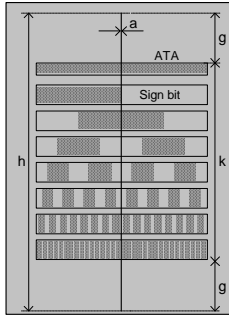


Figure 3: Sketch of digital sun sensor. Notice that the sensor implements Gray codes. a is smaller than the width of the least significant bit (LSB).

3 Sensor Design

Equation (3) for the situation when the illuminated area $A_{t1}(\alpha)$ is increasing, and $A_{t2}(\alpha)$ decreasing, can be found by using the geometry in figure 2:

$$\frac{\Delta I}{I_{ref}} = \frac{(-2(c-l)\tan\alpha_o - 2l\tan\alpha_i - s)k}{2em} \quad (4)$$

$$\alpha_o = \arcsin\left(\frac{n_1}{n_2}\sin(\alpha_i)\right)$$

where $s = b\tan\alpha_i$ is the shadow effect that arises from the thickness b of the slit. $n_1 = 1$ (vacuum) and $n_2 = 1.474$ is the refraction index for Pyrex. Notice that only one of the two α_x is used here, and in the following, since this situation is more easily depicted in graphs.

¹⁰ATA: Automatic Threshold Adjust.

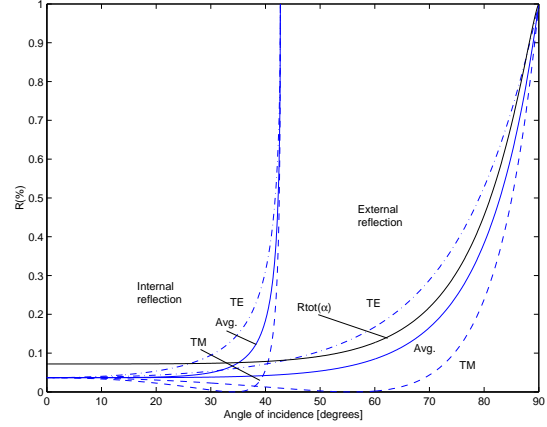


Figure 4: Reflectance in the vacuum-Pyrex transition (external) and the Pyrex-cavity transition (internal). The total reflection from (7) is also shown.

3.1 Reflection and FOV

Not all of the light the sensor is exposed to will reach the active sensor area. Some of the light will be reflected in the vacuum-Pyrex and the Pyrex-cavity transitions. Equation (2) should be multiplied with $(1-R(\alpha))$ where $R(\alpha)$ is the reflection coefficient for both transitions. In (3) and (4) this does not matter since the term here is cancelled out. The reflection is however important in the design.

The reflectance R is defined by $R = \frac{P_r}{P_{in}}$, and deductions from the Fresnel equations in [1] can be rewritten to:

$$R_{TE}(\alpha) = \left(\frac{\cos\alpha - \sqrt{n^2 - \sin^2\alpha}}{\cos\alpha + \sqrt{n^2 - \sin^2\alpha}}\right)^2 \quad (5)$$

$$R_{TM}(\alpha) = \left(\frac{n^2\cos\alpha - \sqrt{n^2 - \sin^2\alpha}}{n^2\cos\alpha + \sqrt{n^2 - \sin^2\alpha}}\right)^2 \quad (6)$$

where $n = \frac{n_1}{n_2}$, and TE/TM the transverse electric/magnetic polarised light waves. In TE/TM the \mathbf{E}/\mathbf{B} vector is perpendicular to the plane of incidence, and the \mathbf{B}/\mathbf{E} vector is in the plane of incidence. Light comes in equal portions of TE and TM modes, which means that the total reflectance in the sensor is¹¹:

$$R(\alpha)_{lm} = \frac{R_{TE}(\alpha)_{lm} + R_{TM}(\alpha)_{lm}}{2}$$

$$R(\alpha) = 1 - (1 - R(\alpha_i)_{12})(1 - R(\alpha_o)_{21}) \quad (7)$$

¹¹It is assumed that the reflected light in the Pyrex-cavity transition will not be reflected back in the vacuum-Pyrex transition.

where subscript 12 and 21 means vacuum-Pyrex and Pyrex-cavity transition respectively. Figure 4 shows the above described reflections.

For the sensor a FOV of $\pm 70^\circ$ was selected since this is well above the required $\pm 55^\circ$. From figure 4 it can also be seen that the total reflection still is relatively low – $< 25\%$ – at this FOV.

3.2 Physical Design

The dimensions of a , e , k , and l in figure 2 are important dimensions for the final characteristics of the device. The device is dimensioned from a desired current at $\alpha = 0^\circ$:

$$I_{t,0^\circ} = \frac{P}{A} \frac{1}{2} ak \eta (1 - R(\alpha)) \Leftrightarrow$$

$$k = \frac{2I_{t,0^\circ} V(T)}{a \frac{P}{A} \eta (1 - R(\alpha))} \quad (8)$$

Large value of k (\Rightarrow narrow slit length a) is needed for large changes in $A_t(\alpha)$, but contrarily wide a is needed for a small reference cell height m . m can also be selected from a desired current at $\alpha = 0^\circ$. e is given from the selected FOV.

Common for all dimensions is that they should be selected in a way such that $\frac{dI}{d\alpha}$ is relatively large for most α angles. Doing this will ensure high sensitivity.

Figure 5 shows that the Pyrex-sensor distance l influences the linearity of the device. l should be selected as low as practically possible.

Table 4 shows the dimensions chosen for the analog sensor. A very conservative design has been selected because short development time and first time success is needed.

Description	Value	
Slit width	a	550 μm
Slit extra length	g	150 μm
Triangle height	k	2405 μm
Triangle width	$2e$	1505 μm
Sensor-Pyrex dist.	l	5 μm
Ref. area height	m	1190 μm
Pyrex thickness	c	500 μm
Al thickness	b	2000 Å

Table 4: Dimensions of the sun sensor.

The Pyrex and SOI wafer are anodically bonded together, which means that l should be large enough to avoid bonding between the Pyrex and the active sensor areas since this will destroy them. The maximum deflection of an $\tilde{a} \times \tilde{b}$ plate with its four sides

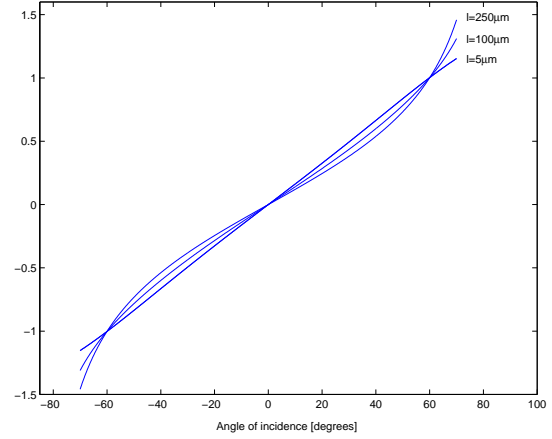


Figure 5: $\frac{\Delta I_t}{I_{ref}}$ graphs. Non-linearity is introduced with $\tan(\alpha_i)$ since $\alpha_i \geq \alpha_o$ in equation (4).

fixed are given in [4]:

$$y_{max} = \frac{\tilde{\alpha} F \tilde{b}^4}{Et^3} \quad (9)$$

where F is a uniform force on top of the entire Pyrex cavity, \tilde{b} the length of the short sides in the rectangle, $E = 64\text{GPa}$ Young's Modulus for Pyrex, and $t = c - l$. $\tilde{\alpha}$ can be determined from tables in [4] to $\tilde{\alpha} = 0.0188$ since $\frac{\tilde{a}}{\tilde{b}} \approx 1.22$ for the sensor. An expression for the force F is deduced in [3]:

$$F = - \frac{\epsilon_g AV^2}{\left(\frac{1}{2}x_d + \frac{\epsilon_g}{\epsilon_0}x_r\right)^2} \quad (10)$$

where A is the area of the Pyrex cavity, V bonding voltage, $\epsilon_g = 4.6\epsilon_0$ permittivity for Pyrex, $x_d = 1\mu\text{m}$ thickness of the depletion layer introduced with the bonding [3], and x_r which is the Pyrex-*Si* gap. Calculations give deflections in the order of $y_{max} = 4\text{pm}$. This shows that the selected l value can be used. That the vents in figure 10 has not been taken into account cannot change y_{max} with a factor 10^6 , since the vents only constitutes a small part of the total bonding area.

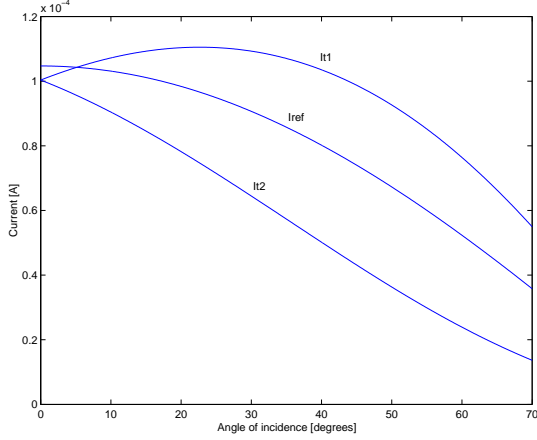


Figure 6: Currents for A_{t1} increasing, A_{t2} decreasing, and I_{ref} .

3.3 Electrical Characteristics

Figure 6 shows the ideal current characteristics of the three sensors. Values used for the characteristics are diode forward voltage $V(T) = 0.7V$, solar cell efficiency $\eta = 0.1$, and average sun intensity $\frac{P}{A} = 1371 \frac{W}{m^2}$. η has been selected low since experience at MIC shows that $\eta = 0.16$ can be obtained quite easily. The maximum efficiency of a pn junction solar cell is $\eta \approx 0.28$ [2]. The earlier discussed $(1 - R(\alpha))$ product is included in characteristics. The illuminated areas used for the graphs are (determined analogues to (4)):

$$A_{t1}(\alpha) = (a - s)(2e + 2(c - l) \tan \alpha_o + 2l \tan \alpha_i + s) \frac{k}{4e}$$

$$A_{t2}(\alpha) = (a - s)(2e - 2(c - l) \tan \alpha_o - 2l \tan \alpha_i - s) \frac{k}{4e}$$

$$A_{ref}(\alpha) = (a - s)m$$

Figure 7 shows the current characteristics for the case when the generated currents in the two triangular cells are subtracted from each other. This can be done by connecting the anodes and cathodes as seen in figure 16.

A signal proportional to ΔI_t is divided by a signal proportional to I_{ref} . This gives the linear graph in figure 8. Figure 9 shows the derivatives of these currents. From this figure it is seen that the current change rate is very low around 0° for I_{ref} , and $\sim 50^\circ$ for ΔI_t . Close to these angles measurements are more vulnerable to noise. However, this is not expected to be a problem since the curves are relatively steep.

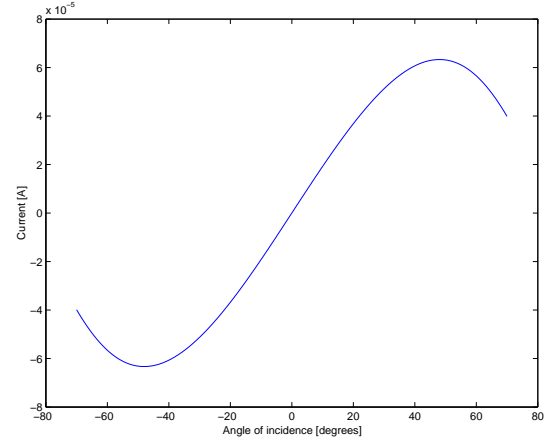


Figure 7: The subtracted current ΔI_t .

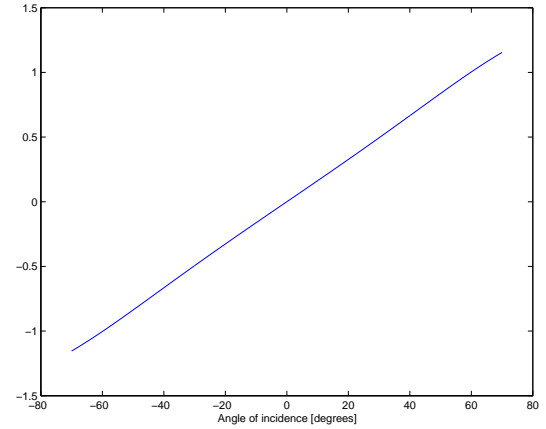


Figure 8: Signal $\frac{\Delta I_t}{I_{ref}}$.

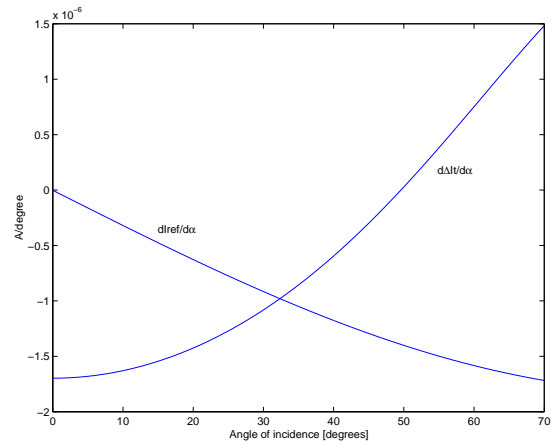


Figure 9: Derivatives $\frac{d\Delta I_t}{d\alpha}$ and $\frac{dI_{ref}}{d\alpha}$.

4 Sensor Realisation

Figure 10 shows the mask layout for the analog sensor. Figure 11 shows the needed masks, and their mutual alignment relationship – that is which mask shall the individual masks be aligned to in the photolithographic processes.

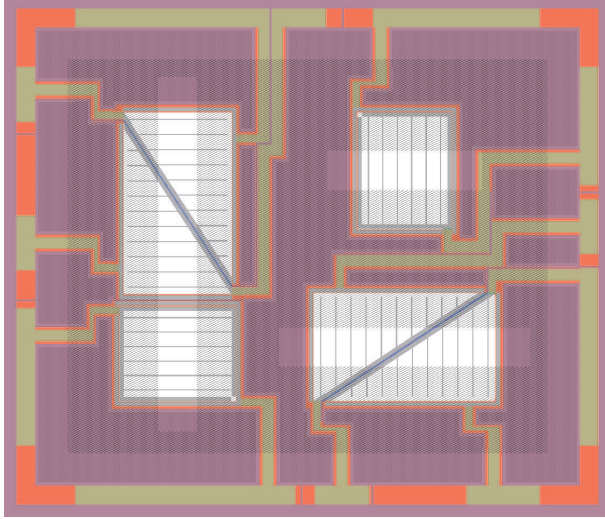


Figure 10: Masks for the analog sensor. The seven masks are superimposed on top of each other. Version with contact fingers.

Mask M1 is needed to form the pn junctions in the p-type substrate. M2 is needed to lower the Schottky barrier between the p-substrate and the contact metal, since the generated photo current will encounter this Schottky diode in its reverse direction. The Schottky barrier height is given by $\phi_{Bp} = V_{bi} + \phi_p$, where V_{bi} is the built-in potential and ϕ_p the potential between the Fermi level and the top of the valence band. Assuming complete ionisation yields hole concentration $p_0 \approx N_a$ (N_a acceptor doping):

$$\phi_{Bp} \approx V_{bi} + \frac{kT}{e} \ln \left(\frac{N_v}{N_a} \right) \quad (11)$$

This means that the Schottky barrier can be lowered by increasing the p doping under the metal contacts – the effective density of states in the valence band N_v is a fixed number for Si . The physical effect of increasing the doping is that the space charge region decreases, which enables carrier tunnelling and hence a better ohmic contact.

The conducting paths to the n well has to be insulated from the p well, and vice versa. This is

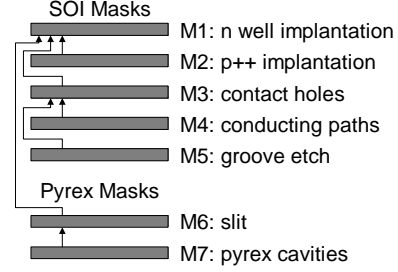


Figure 11: Needed masks, and their alignment relationship.

done by having an oxide layer between the wafer and the conducting paths. To obtain contacts to the n and p wells mask M3 is needed for etching contact holes. M4 is needed to define a pattern for conducting paths. M5 is used to etch off the device layer between the active sensor areas to ensure electrical insulation.

On the Pyrex wafer the slit has to be created with e.g. metals. Mask M6 allows this, and M7 defines the pattern needed for cavity etching in the bottom side of the Pyrex wafer.

The implemented mask design is based on the measures from table 4. As mentioned earlier the design is very conservative to allow first time success and short development time. As a result of this large tolerances are included. Misalignments of $5\mu\text{m}$ is allowed for photolithographic steps, and $50\mu\text{m}$ for the bonding alignment.

For further enhancement of robustness the bonding pads has been made large enough to hold at least three wire bondings. Cavities are made in the Pyrex above the conducting paths. These will act as vents in the air to vacuum transition during launch.

Two versions of the analog sensor are under fabrication. One with and one without contact fingers on top of the active areas. The fingers, which covers 5% of the active area, decrease the resistance experienced by the generated photo current. Because of the small device size it is expected that the finger version only will have a slightly higher η . The finger version is mostly included for test purposes since it is expected that the version without fingers will be used – it will have higher sensitivity since it has no finger shadows.

In addition to the sensors several test patterns and alignment marks are of course included. Test patterns allow e.g. SIMS¹², ellipsometer, and stylus type profiler tests.

¹²SIMS: Secondary Ion Mass Spectrometry.

The Digital Sensor

The developed masks and process sequence allows fabrication of the analog and digital sensors on the same wafers. Figure 12 shows the mask layout for the digital sensor.

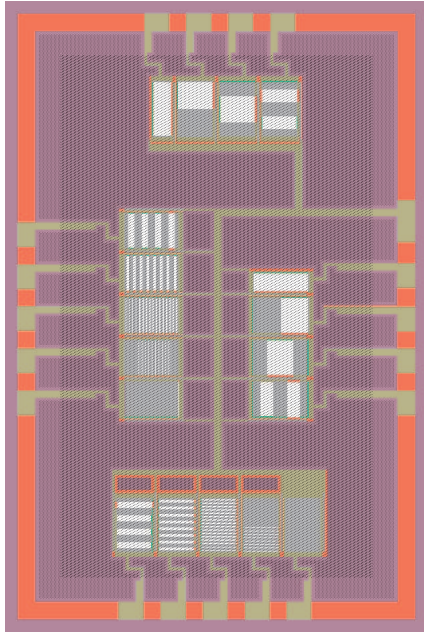


Figure 12: Masks for the digital sensor.

4.1 Process Sequence

The actual process sequence used for the fabrication consists of more than forty steps. However in the following only the main steps are described. Drawings are not to scale. Simple steps like photolithography with different polarity and numerous cleaning and verification steps are left out. Used notation:

 Low doped Si	 Thermal oxide	 Silicon nitride
 n ⁺ doped Si	 p ⁺⁺ doped Si	 Pyrex
 Ti/Al	 Cr/Au	

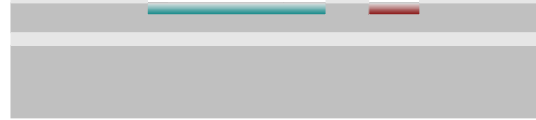
500 μ m SOI substrate, p-type device layer.



A thin thermal oxide is grown.



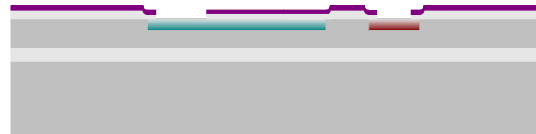
A two step implantation process creates the diode (pn junction) and ohmic contacts to the p-layer.



A passivation layer and an antireflective coating is created by further thermal oxidation and LPCVD¹³ silicon nitride. The two processes also activates the implanted ions by annealing them into the lattice.



Contact holes are opened by RIE¹⁴.



Electrical conduction paths from the diode to the wire bonding pads are created by E-beam evaporation of titanium/aluminium and a lift off process. *Ti* is used as an adhesive layer for *Al* and prevents the latter from diffusing into the silicon.



The devices are electrically separated by RIE.



500 μ m Pyrex wafer.



¹³LPCVD: Low Pressure Chemical Vapour Deposition.

¹⁴RIE: Reactive Ion Etch.

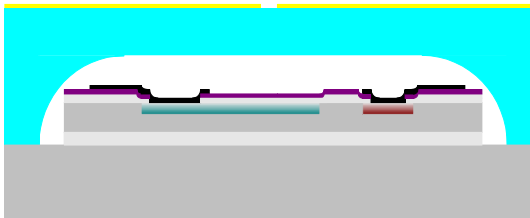
The optical slits are created by E-beam evaporated chromium/gold and a lift off process.



Cavities for the diode are etched in the Pyrex wafer with HF -acid.



The SOI substrate are anodically bonded to the Pyrex wafer prior to the dicing.



Anodic bonding is a suitable bonding method for space applications since normal adhesives can be avoided – thus allowing a more uniform interface. With anodic bonding the interface between the two wafers becomes a chemical structure of SiO_2 molecules. This is obtained by applying an electrical field over the two wafers with the anode on the Pyrex wafer; see figure 13. Thereby pulling mobile Na^+ ions away from the interface, hence creating a strong electrostatic attraction between the Pyrex and the silicon wafer. By performing this procedure at $350^\circ C$ the mobility of positive ions are increased which, combined with the electrical field, transports oxygen in the Pyrex to the interface creating $Si-O-Si$ bonds between the two wafers. The process is irreversible and hence creates a permanent bond.

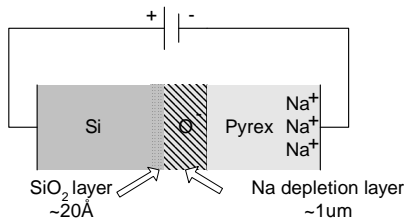


Figure 13: Anodic bonding.

The final step in the fabrication is the dicing of the wafer stack, which is done by using a high precision diamond saw. Figure 14 shows how the chips are diced.

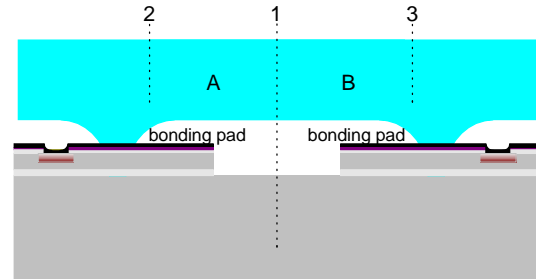


Figure 14: Dicing method.

It is necessary to saw three lines, where line no. 1 separates the different chips. Lines no. 2 and 3 are cut in the Pyrex to remove segments A and B, and thereby making the underlying bond pads accessible.

5 Sensor Circuit

The circuit have to fulfil the specifications given for DTU_{sat}, and convert the signals from the sensor to a useful measuring range. The general requirements are to minimise the power consumption and mass of the circuit, but also the number of Input/Output channels has to be kept down to minimise harness complexity. To minimise noise the necessary amplification and conversion electronics have to be situated close to the sensor.

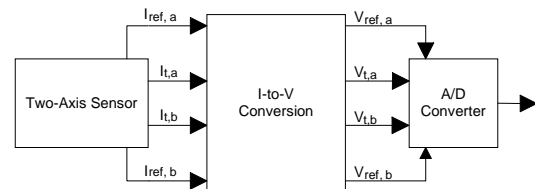


Figure 15: Block diagram for one sensor chip.

Figure 15 shows a block diagram of the sensor circuit where I_t is the current difference from the triangular sensor areas, and I_{ref} is the current from the reference element; sensors a and b are perpendicular.

Current to voltage conversion is implemented with op amps as shown in figure 16. Connecting the two triangular photo diodes in parallel with opposite orientations produces the differential current, where the common mode current circulates in the diode

loop resulting in no signal output. This way of connecting the diodes directly across the zero voltage of the op amp’s differential inputs removes diode leakage and the associated offset result. Furthermore the CMR¹⁵ of coupled noise is ensured by the impedance connected to the op amps’ inputs.

The necessary division of the output voltage is realised using an A/D converter where the reference input determines the span of the converter and thereby acts as a divider. The division can be carried out in software, but this results in lower resolution since non-linear signals then has to be digitised, see figure 7. A bipolar converter is used in order to eliminate offset errors. The reference voltage is generated by a simple current to voltage conversion employed on the output of the reference cell.

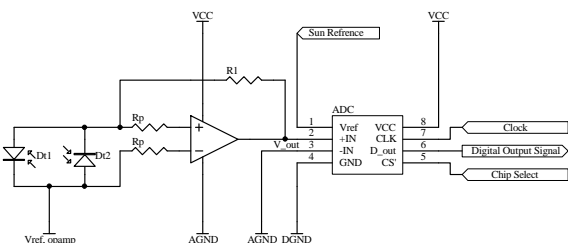


Figure 16: Schematic for one axis of the sensor.

The selected driver circuit is chosen due to its low complexity. The bandwidth of the circuit is relatively low compared with a configuration employing three op amps per sensor axis, but since the measurement is a DC measurement this is actually an advantage.

The division will result in a false angle if the calculation is performed when the sensor is not illuminated. To prevent this situation a sun detector circuit is implemented, which compares a certain threshold to the output voltage for the I-V conversion. This is carried out with a simple comparator circuit.

The six different two-axis sensors are activated sequentially from the ACDS main board by powering up the needed sensor amplifiers. Each axis are then selected with the chip select on the A/D converter, which activates it on a SPI¹⁶ bus.

A two-sided PCB of 2.4cm×2.8cm including the two-axis sensor and the described circuits has been designed with a mass just below 3g.

¹⁵CMR: Common Mode Rejection.

¹⁶SPI: Serial Peripheral Interface.

Resolution

Resolution of the described circuit depends mainly on the noise introduced by the op amp and to some extent the A/D converter. Hence the op amp should have features such as low offset voltage, drift and input bias current besides the requirements and constraints induced by the environment. Low supply current, small integral linearity error, and auto shut-down are the key features for the A/D converter.

An estimate of the resolution based on typical specifications for high performance rail-to-rail op amps and bipolar A/D converters is given in the following.

The total noise introduced by the op amp driven on a 3V single supply is approximated to $V_n = 55\mu V$, which arises from offset and bias currents. The integral linearity error of a 12-bit A/D converter is around $\pm \frac{3}{4} LSB$. This yields, with a minimum reference voltage of 250mV, a total noise of:

$$\begin{aligned} V_{noise,max} &= 0.75V_{LSB} + V_n \\ &= 0.75 \cdot \frac{250mV}{4096} + 55\mu V \\ &= 101\mu V \end{aligned}$$

It can be concluded that a resolution of 11bit is obtainable, where $V_{LSB} = 122\mu V$ leaving $21\mu V$ for noise from the supply and the op amp reference voltage. The power supply rejection ratio is around 120dB implying that a supply ripple can be neglected. Hence the requirement to the op amp reference voltage noise is that it should be below $21\mu V$. The 11-bit effective resolution leads to the following angular resolution for a $\pm 70^\circ$ FOV:

$$\frac{140^\circ}{2048} = 0.07^\circ$$

6 Mechanical Integration

The considered mechanical integration of the sensor is shown in figure 17. The sensor chip is placed on a chip carrier, which is soldered to the PCB. To ensure chip-PCB alignment, a spacer is employed between the chip carrier and the PCB. The PCB is aligned to the exterior of the satellite.

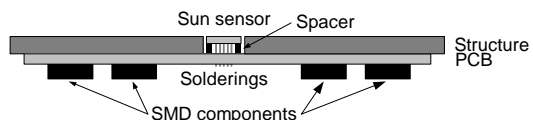


Figure 17: Placement of the sensor in the satellite.

7 Future Work

Design and process validation is finished. Final masks have been produced, and the production of the first prototypes has been initiated.

The first prototype and its characteristics is expected to be ready mid July. Additional electronics will be developed to test the full potential of the developed sensors. After this milestone calibration and production of a second prototype will be started.

A first engineering model will be ready in the end of August, where the first engineering model of DTUsat is assembled. Before this the sensor will undergo environmental and shock/vibration tests.

8 Conclusion

A two-axis MOEMS sun sensor with $\pm 70^\circ$ FOV, and a theoretical resolution of 0.07° has been designed for DTUsat. The sensor has been made independent of various ambient factors. A complete system consisting of the sensor and required electronics has been designed with a mass just below 3g. Implying that mass constrained missions clearly can benefit by employing a MOEMS sun sensor, without compromising accuracy.

9 Acknowledgements

Prototype costs are being sponsored by Mikroelektronik Centret (MIC), and the DTUsat project is partially funded by the Public Space Research Committee; under the Ministry of Science, Technology and Innovation. Several companies have also contributed to various task groups within DTUsat.

The authors would like to thank: Their advisor Process Specialist M.Sc. René Fléron (MIC). Their advisor on earlier DTUsat projects Professor Mogens Blanke (Dep. of Automation, Ørsted•DTU). M.Sc. students Torsten Lorentzen and especially Klaus Krogsgaard for great collaboration in the overall design of the ACDS. Oticon for financial support to this conference. The entire DTUsat group for the joint effort.

References

- [1] S.J. Frank L. Pedrotti and Leno S. Pedrotti. *Introduction To Optics*. Prentice Hall, 1993.
- [2] Donald A. Neamen. *Semiconductor Physics & Devices*. Irwin/McGraw-Hill, 1997.
- [3] Steen Weichel. *Silicon to Silicon Wafer Bonding for Microsystem Packaging and Formation*. PhD thesis, Mikroelektronik Centret (MIC) at The Technical University of Denmark, 2000.
- [4] W.C. Young. *Roark's Formulas for Stress and Strain*. McGraw-Hill, New York, 1989.